Dynamic equilibrium between closed and partially closed states of the bacterial Enzyme I unveiled by solution NMR and X-ray scattering

Vincenzo Venditti[a,b,1], Charles D. Schwieters[c,1], Alexander Grishaev[a,2], and G. Marius Clore[a,3]

[a]Laboratory of Chemical Physics, National Institute of Diabetes and Digestive and Kidney Diseases, National Institutes of Health, Bethesda, MD 20892-0520; [b]Department of Chemistry, Iowa State University, Ames, IA 50011; and [c]Division of Computational Biosciences, Center for Information Technology, National Institutes of Health, Bethesda, MD 20892-5624

Contributed by G. Marius Clore, August 4, 2015 (sent for review July 27, 2015; reviewed by Hashim M. Al-Hashimi)

Enzyme I (EI) is the first component in the bacterial phosphotransferase system, a signal transduction pathway in which phosphoryl transfer through a series of bimolecular protein–protein interactions is coupled to sugar transport across the membrane. EI is a multidomain, 128-kDa homodimer that has been shown to exist in two conformational states related to one another by two large (50–90°) rigid body domain reorientations. The open conformation of apo EI allows phosphoryl transfer from His189 located in the N-terminal domain α/β ($EIN^{\alpha/\beta}$) subdomain to the downstream protein partner bound to the EIN^{α} subdomain. The closed conformation, observed in a trapped phosphoryl transfer intermediate, brings the $EIN^{\alpha/\beta}$ subdomain into close proximity to the C-terminal dimerization domain (EIC), thereby permitting in-line phosphoryl transfer from phosphoenolpyruvate (PEP) bound to EIC to His189. Here, we investigate the solution conformation of a complex of an active site mutant of EI (H189A) with PEP. Simulated annealing refinement driven simultaneously by solution small angle X-ray scattering and NMR residual dipolar coupling data demonstrates unambiguously that the EI(H189A)–PEP complex exists in a dynamic equilibrium between two approximately equally populated conformational states, one corresponding to the closed structure and the other to a partially closed species. The latter likely represents an intermediate in the open-to-closed transition.

multidomain protein dynamics | dipolar couplings | X-ray scattering | conformational states | ligand binding

Enzyme I (EI) is the first component of the bacterial phosphoenolpyruvate (PEP):sugar phosphotransferase signal transduction system (PTS) whereby transfer of sugars across the membrane is coupled to a sequential phosphorylation cascade involving a series of bimolecular protein–protein interactions (1). Autophosphorylation of EI by PEP activates the PTS. Under conditions of nitrogen limitation, competitive inhibition of EI by α-ketoglutarate, an analog of PEP, abolishes sugar uptake by the PTS, thereby providing a regulatory link between central carbon and nitrogen metabolism (2, 3).

EI is a 128-kDa homodimer, with each subunit comprising two domains (4–6) (Fig. 1*A*). The N-terminal domain (EIN) is itself subdivided into two subdomains: EIN^{α} includes the binding site for the His phosphocarrier protein (HPr), the downstream partner in the phosphorylation cascade, and $EIN^{\alpha/\beta}$ contains the site of phosphorylation at His189 (7–9). The C-terminal dimerization domain (EIC) possesses the PEP binding site (10–13). EIN^{α} and $EIN^{\alpha/\beta}$ are connected to one another by two extended loops (7–9), whereas $EIN^{\alpha/\beta}$ is connected to EIC via a long swivel helix (14, 15) (Fig. 1*A*). The structures of free EI from *Escherichia coli* and *Staphylococcus aureus* in solution (16, 17) and crystal states (15) display open conformations (Fig. 1*A*, *Left*), whereas the structure of a trapped phosphoryl transfer intermediate of phosphorylated *E. coli* EI has a closed conformation (14) (Fig. 1*A*, *Right*). The open-to-closed state transition involves two large rigid body conformational transitions accompanied by an ∼50–70° reorientation of $EIN^{\alpha/\beta}$ relative to EIC and an ∼90° reorientation of EIN^{α} relative to $EIN^{\alpha/\beta}$ (16). We refer to the $EIN^{\alpha}/EIN^{\alpha/\beta}$ orientation found in the open and closed structures as the A and B conformations of EIN, respectively. Only the A conformation has been observed in solution and crystal structures of isolated EIN, free (7, 8), complexed to HPr (9), or phosphorylated (18). Modeling suggests that either both domain reorientations occur concurrently or reorientation of $EIN^{\alpha/\beta}$ relative to EIC precedes reorientation of EIN^{α} to avoid a steric clash between EIN^{α} and EIC, resulting in the formation of an intermediate (16).

In the closed structure, the position of $EIN^{\alpha/\beta}$ relative to EIC allows direct in-line phosphoryl transfer from PEP bound to EIC to His189 on $EIN^{\alpha/\beta}$ (14). However, in the orientation of EIN^{α} relative to $EIN^{\alpha/\beta}$ seen in the closed state (i.e., the B conformation of EIN) the Cα-Cα distance between His189 and His15 of HPr bound to EIN^{α} is too large (∼30 Å) to permit subsequent phosphoryl transfer from EIN to HPr (16). In the open state of EI, with EIN in the A conformation, however, the reverse holds: the orientation of EIN^{α} to $EIN^{\alpha/\beta}$ places His189 in close proximity to His15 of HPr, thereby permitting in-line phosphoryl transfer to HPr (9). Thus, rapid interconversion between the open and closed states of EI is critical to catalytic function.

Significance

The bacterial phosphotransferase system couples phosphoryl transfer to sugar transport across the cell membrane. The first protein in the pathway, Enzyme I (EI), undergoes two large rigid body domain reorientations between an autophosphorylation-competent closed state and an open state that allows subsequent phosphoryl transfer to its downstream protein partner. Simultaneous use of solution X-ray scattering and NMR dipolar coupling data to guide simulated annealing refinement reveals the existence of a dynamic equilibrium between closed and partially closed conformations in a complex of a mutant of EI with phosphoenolpyruvate. The partially closed conformation represents an intermediate in the open-to-closed transition.

Author contributions: V.V., C.D.S., and G.M.C. designed research; V.V., C.D.S., and A.G. performed research; V.V., C.D.S., and G.M.C. analyzed data; and V.V., C.D.S., and G.M.C. wrote the paper.

Reviewers included: H.M.A., Duke University Medical Center.

The authors declare no conflict of interest.

Data deposition: The atomic coordinates, experimental RDC and SAXS data, and chemical shift assignments have been deposited in the Protein Data Bank, www.pdb.org (PDB ID code 2N5T).

[1]V.V. and C.D.S. contributed equally to the work.

[2]Present address: Institute of Bioscience and Biotechnology Research, University of Maryland, Rockville, MD 20850.

[3]To whom correspondence should be addressed. Email: mariusc@mail.nih.gov.

This article contains supporting information online at www.pnas.org/lookup/suppl/doi:10.1073/pnas.1515366112/-/DCSupplemental.

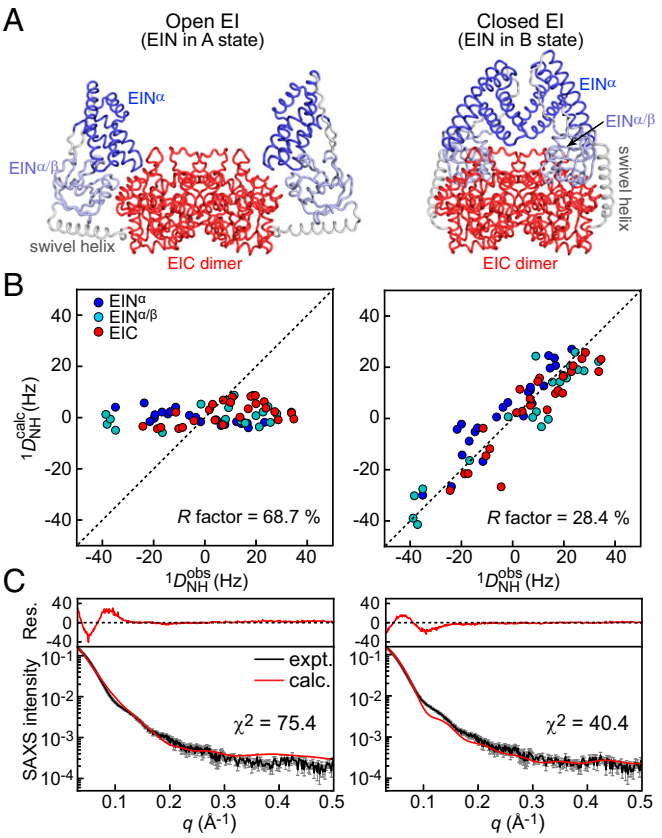

Fig. 1. Agreement of the experimental RDC and SAXS data acquired for the EI^{A}–PEP complex with the EI^{open} and EI^{closed} structures. (*A*) NMR structure of EI^{open} [*Left*; PDB ID code 2KX9 (16)] and X-ray structure of EI^{closed} [*Right*, trapped phosphoryl transfer intermediate; PDB ID code 2HWG (14)]. EIN^{α}, $EIN^{\alpha/\beta}$, and EIC are colored blue, light blue, and red, respectively. (*B*) Agreement between the experimental ($^{1}D_{NH}^{obs}$) RDCs for the EI^{A}–PEP complex and the back-calculated ($^{1}D_{NH}^{calc}$) RDCs for the EI^{open} (*Left*) and EI^{closed} (*Right*) structures obtained by predicting the alignment tensor from molecular shape. Data points are colored blue, light blue, and red for EIN^{α}, $EIN^{\alpha/\beta}$, and EIC, respectively. (*C*) Agreement between experimental SAXS curve (black) for the EI^{A}–PEP complex and the back-calculated curves (red) for the EI^{open} (*Left*) and EI^{closed} (*Right*) structures. The residuals, given by $(I_i^{calc} - I_i^{obs})/I_i^{err}$, are plotted above the SAXS curves. Error bars: 1 SD.

We recently showed that the open/closed interconversion of PEP-bound EI is modulated by the volume of the active site side chain at position 189, with smaller side chains favoring the closed conformation (19). In the wild-type EI (EI^{WT})–PEP complex, the latter is undetectable in solution by small angle X-ray scattering (SAXS) (19) despite the fact that the closed conformation could be selectively crystallized from a solution of EI, PEP, and Mg^{2+} in which the autophosphorylation reaction was quenched by the inhibitor oxalate (14). These observations can be attributed to steric and electrostatic repulsion between phosphorylated His189 and bound PEP (19), and they emphasize that the crystallized phosphoryl transfer intermediate represents a sparsely populated state in solution. No such clash exists for the EI(H189A) mutant (EI^{A}), and initial SAXS analysis suggests that the EI^{A}–PEP complex is skewed toward the closed conformation (~60%); however, a mixture of closed and open states does not accurately reproduce the observed SAXS curve (19) or fully account for the residual dipolar coupling (RDC) data measured by NMR (this work).

Here, on the basis of the known structures of the individual domains of EI, we investigate the solution structure of the EI^{A}–PEP complex by rigid body-simulated annealing refinement driven by experimental RDC and SAXS data. This analysis indicates that the EI^{A}–PEP complex exists as a rapidly interconverting ensemble of two approximately equally populated conformations comprising closed and partially closed states, and it suggests a functional role for the partially closed state in PEP binding and subsequent pyruvate release following autophosphorylation.

Results and Discussion

RDC Analysis of the Individual Structural Domains. RDCs measure the orientation of bond vectors relative to an external alignment tensor, and therefore provide a very sensitive indicator of both structural quality (20) and relative domain orientations (21). Backbone amide ($^{1}D_{NH}$) RDCs for uniformly $^{15}N/^{2}H$-labeled EI^{A}–PEP complex, aligned in a neutral bicelle medium (22), were measured for well-resolved $^{1}H_N/^{15}N$ cross-peaks in the ^{1}H-^{15}N transverse relaxation optimized spectroscopy (TROSY) correlation spectrum using the ARTSY (amide RDCs by TROSY) technique (23) (the distribution of measured RDCs is shown in Fig. S1). As in the case of EI^{WT} (16), the observed RDCs for the EIN^{α} and $EIN^{\alpha/\beta}$ subdomains of the EI^{A}–PEP complex, treated separately, agree better with the corresponding coordinates from the solution NMR structure of the EIN–HPr complex [Protein Data Bank (PDB) ID code 3EZA (9)] (Table 1) than with the corresponding coordinates from the X-ray structures of either isolated EIN (7) or the full-length EI phosphoryl transfer intermediate [PDB ID code 2HWG (14)]. This improved agreement is simply a reflection of the fact that the structure of the EIN–HPr complex was determined using RDCs, albeit in a charged alignment medium of phage fd (9) (hence, the excellent agreement of

Table 1. SVD analysis of backbone amide ($^{1}D_{NH}$) RDCs for the EI^{A}–PEP complex

Domain	No. of RDCs	D_a^{NH} (Hz)	η	*R*-factor,* %
EIN^{α}	23	−19.3	0.34	**21.8**
$EIN^{\alpha/\beta}$	20	−19.7	0.47	**17.7**
$EIN^{A\text{-state}}$	43	−16.5	0.37	50.9
$EIN^{B\text{-state}'}$	43	−19.5	0.37	**22.2**†
$EIN^{B\text{-state}''}$	43	−19.6	0.37	**22.0**†
$EIC^{monomer}$	25	−21.8	0.27	**24.6**
EIC^{dimer}	25	−22.3	0.28	**25.0**
EI^{open}	68	−5.8	0.46	53.5
EI^{open}‡	68	4.3	0.36	68.7
EI^{closed}	68	−21.2	0.27	**25.8**
EI^{closed}‡	68	−20.8	0.47	28.4

SVD analysis was carried out using the calcTensor helper of Xplor-NIH (29). The base coordinates for the two subdomains of EIN are taken from the solution structure of the isolated EIN–HPr complex [PDB ID code 3EZA (9)]. The structure of isolated EIN (7–9), as well as the structure of EIN in the context of free intact EI (15, 16), is in the A conformation. The coordinates of the B conformation of EIN observed in the crystal structure of the phosphoryl transfer intermediate (14) were obtained by best-fitting the backbone atoms of the EIN^{α} and $EIN^{\alpha/\beta}$ subdomains from the solution structure [PDB ID code 3EZA (9)] onto the crystal structure of phosphorylated EI [PDB ID code 2HWG (14)]. The coordinates of EIC and the swivel helix were taken from the crystal structure of phosphorylated EI (PDB ID code 2HWG), with protons added using Xplor-NIH (29).

*RDC *R*-factor is given by $[<(D_{obs} - D_{calc})^2>/(2<D_{obs}^2>)]^{1/2}$, where D_{obs} and D_{calc} are the observed and calculated RDCs, respectively (30). *R*-factors for fits showing good agreement between the coordinates and experimental RDCs are shown in bold. D_a^{NH} (in units of Hz) and η are the magnitude of the axial component of the alignment tensor and the rhombicity, respectively.

†Orientation of the EIN^{α} subdomain relative to the $EIN^{\alpha/\beta}$ subdomain is slightly different (by a rotation of 5.4°) in the two subunits of the X-ray structure of phosphorylated EI (14); SVD analysis was therefore performed separately for the two subunits (denoted as ′ and ″).

‡These results were calculated using the SARDC facility in Xplor-NIH (29), which computes the alignment tensor from molecular shape rather than using it as a set of fit parameters as in the case of SVD.

Table 2. RDC and SAXS analysis of the EI^A–PEP complex

Structure	RDC *R*-factor, %				SAXS*
	EIN^{α}	$EIN^{\alpha/\beta}$	EIC	EI	χ^2
Back-calculation of RDC and SAXS data from the EI^{open} and EI^{closed} structures†					
EI^{open}	79.0	67.2	62.6	68.7	75.4
EI^{closed}	35.1	23.0	29.8	28.4	43.5
EI^{mix}‡	34.2	24.7	34.6	30.2	36.8
Structure refinement of EI^A–PEP complex against RDC and SAXS data§					
$N_e = 1^{(SAXS)}$	72.0 ± 0.1	70.2 ± 0.5	62.0 ± 0.6	68.1 ± 0.4	2.1 ± 0.1
$N_e = 1^{(RDC)}$	22.3 ± 0.1	19.1 ± 0.1	25.3 ± 0.1	22.0 ± 0.1	30.3 ± 9.4
$N_e = 1^{(RDC/SAXS)}$	25.0 ± 0.3	19.9 ± 0.2	25.2 ± 0.0	23.0 ± 0.1	6.7 ± 0.2
$N_e = 2^{(RDC/SAXS)}$¶	22.3 ± 0.1	20.1 ± 0.1	25.4 ± 0.1	22.4 ± 0.1	1.0 ± 0.0
$N_e = 3^{(RDC/SAXS)}$¶	22.0 ± 0.0	19.4 ± 0.1	25.5 ± 0.1	22.1 ± 0.1	1.0 ± 0.0

Numbers of RDCs are 23 for EIN^{α}, 20 for $EIN^{\alpha/\beta}$, 25 for EIC, and 68 for the whole EI. Target values of the RDC *R*-factors for EIN^{α}, $EIN^{\alpha/\beta}$, and dimeric EIC, obtained by SVD against the corresponding coordinates, are 21.8%, 17.7%, and 25.0%, respectively (Table 1). The target value for the complete EI dimer, given by the weighted average of the RDC *R*-factors for the individual domains, is 21.8%. The target value of χ^2 for the SAXS data is 1.0.

*SAXS curves were back-calculated from the coordinates of the EI structures using the calcSAXS-bufsub helper function (19) of Xplor-NIH (29).

†RDCs arising from steric alignment were back-calculated from the molecular shapes generated from the coordinates of the EI structures using the calcSARDC helper function of Xplor-NIH (29).

‡EI^{Mix} is a two-member ensemble of EI^{open} and EI^{closed} with optimized populations of 5% and 95%, respectively.

§Average values and corresponding SDs over the 10 lowest target function structures are reported.

¶For the $N_e = 2$ ensemble, one member of the ensemble is fixed to the structure of EI^{closed} (14); in the other ensemble member, EIN^{α}, $EIN^{\alpha/\beta}$, and dimeric EIC are allowed to move relative to one another as rigid bodies, by giving residues within the linker regions Cartesian degrees of freedom (main text). Optimized populations for the closed and partially closed members of the ensemble are 51.7 ± 1.1% and 48.3 ± 1.1%, respectively. For the $N_e = 3$ ensemble, a third member, fixed to the coordinates of EI^{open} (16), is added; the optimized populations are 54.5 ± 1.1% (partially closed), 43.1 ± 1.2% (closed), and 2.4 ± 0.1% (open). Structures of $EI^{partially\ closed}$ in the $N_e = 2$ and $N_e = 3$ ensembles are the same within experimental error: when fit to the EIC dimer, the C^{α} rms difference between the EIN domains of the $N_e = 2$ and $N_e = 3$ partially closed structures is only 1.3 ± 0.2 Å.

the RDCs measured in bicelles provides independent cross-validation of the structure), whereas the two crystal structures (7, 14) were solved at a relatively modest resolution (2.5–2.7 Å). Consequently, the NMR coordinates (PDB ID code 3EZA) for EIN^{α} and $EIN^{\alpha/\beta}$ were used for all subsequent analyses and to generate the EIN portion of the closed and open structures, whereas the X-ray coordinates (PDB ID code 2HWG) were used for EIC and the swivel helix (footnotes for Table 1 and *SI Materials and Methods*).

Singular value decomposition (SVD) fits of the $^1D_{NH}$ RDCs obtained for the EI^A–PEP complex to the B-conformation of EIN [i.e., the conformation found in the closed X-ray structure (14)] yields RDC *R*-factors that are only slightly worse than the weighted average of the RDC *R*-factors for EIN^{α} and $EIN^{\alpha/\beta}$ individually (~22% vs. ~20%), with comparable values for the magnitude of the axial component (D_a^{NH}) and rhombicity (η) of the fitted alignment tensors (Table 1). By way of contrast, the A conformation of EIN found in apo EI [open state (16, 17)] and isolated EIN (7–9, 18) results in very poor agreement with the measured RDCs, with an RDC *R*-factor of ~51% (Table 1). Thus, EIN in the EI^A–PEP complex must adopt a conformation or ensemble of conformations that is close to the conformation or ensemble of conformations of the B form found in the closed X-ray structure.

Although no solution structure has been determined for EIC, there is excellent agreement between the measured RDCs for the EI^A–PEP complex and the RDCs back-calculated from the crystal structure of phosphorylated EI (14) with comparable *R*-factors (~25%; Table 1) for both an individual subunit and the dimer. These results are fully consistent with previous RDC data obtained for isolated EIC (13), and indicate that the relative orientation of the two EIC domains in the dimeric EI^A–PEP complex is the same as the relative orientation in the crystal structure of phosphorylated EI (14).

RDC and SAXS Analysis of the Full-Length EI^A–PEP Complex. SVD fits of the $^1D_{NH}$ RDCs measured for the EI^A–PEP complex yield *R*-factors of ~54% and ~26% for the open and closed structures of full-length dimeric EI, respectively (Table 1). The latter RDC *R*-factor, however, is significantly larger than the weighted *R*-factor (~22%) obtained when fitting the domains individually. Because the RDCs were measured in a medium (neutral bicelles) where alignment is induced through transient steric interactions, the alignment tensor can be calculated from molecular shape and the RDCs can be back-calculated directly from the molecular coordinates (24–26). Although this approach results in a slightly poorer fit for the closed structure (*R*-factor ~28%; Fig. 1*B*, *Right*), the values of D_a^{NH} and η are close to the values obtained from SVD analysis (Table 1). In contrast, the value of D_a^{NH} predicted from the open structure is fivefold smaller and of opposite sign (Table 1), and there is no agreement between observed and back-calculated RDCs (*R*-factor ~69%; Fig. 1*B*, *Left*). One can therefore conclude that the EI^A–PEP complex adopts a conformation(s) that is similar to the conformation of the closed structure.

SAXS, however, reveals a more complex picture, because neither the open (χ^2 ~75) nor closed (χ^2 ~44) structures of EI are consistent with the experimental SAXS curve for the EI^A–PEP complex (Fig. 1*C* and Table 2). Moreover, a linear combination of open and closed structures (with optimized populations of 5% and 95%, respectively) results in only minimal improvement, in agreement with the experimental SAXS data (χ^2 ~37; Table 2) and a slight worsening of the agreement with the RDC data (*R*-factor ~30%), indicating that a simple two-state equilibrium between open and closed structures does not represent the state of the EI^A–PEP complex in solution.

Structure Refinement of the EI^A–PEP Complex. To determine the 3D structure of the EI^A–PEP complex in solution, we therefore made use of RDC- and SAXS-driven rigid body simulated

annealing in which EIN$^{\alpha}$, EIN$^{\alpha/\beta}$, and the EIC dimer were treated as separate rigid bodies, whereas the linker regions connecting EIN$^{\alpha/\beta}$ to EIN$^{\alpha}$ (residues 22–24 and 143–146) and EIC (residues 255–261) were given Cartesian degrees of freedom (full details of the calculational strategy are provided in *SI Materials and Methods*). Allowing backbone deformations of the rigid bodies is not justified because agreement between observed and calculated RDCs at the individual subdomain/domain level (as discussed above) is within the error of the measured RDCs and structure coordinates.

Similar calculations were used to investigate the solution structure of EI^{WT} (16) and the EI(H189Q) mutant (17). However, in the current work, the RDC alignment tensor was calculated directly from the coordinates and molecular shape at every step of molecular dynamics and minimization, as was described in our recent work on the HIV-1 capsid protein (26). This aspect of the calculations is critical because it enables one to carry out ensemble calculations where a single structure is insufficient to account for the experimental data. Further, this approach makes full use of the information content present in the RDCs because both molecular shape and bond vector orientations are taken into account. In addition, considerable speedup in the computation of SAXS curves was achieved by decomposition into a small number of rigid bodies, thereby rendering the calculation independent of the number of atoms. Specifically, for atoms within a rigid body, the relative atom positions do not change; thus, after an initial calculation, the corresponding contribution to the scattering amplitude can be computed without referring to atomic positions (details are provided in *SI Materials and Methods*).

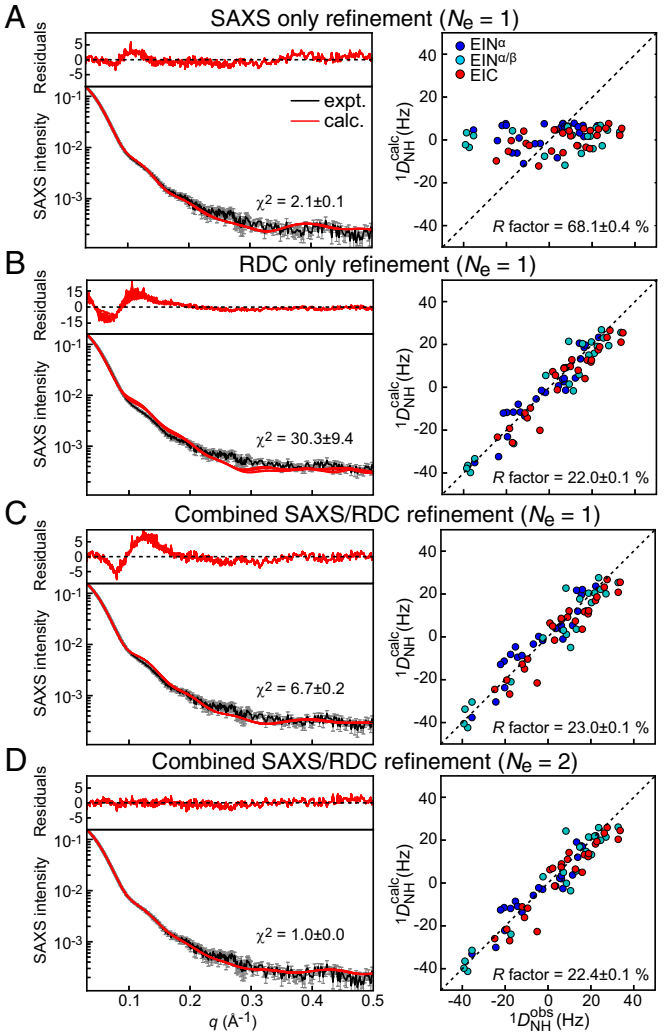

Fig. 2. Structure refinement of the EI^{A}–EP complex. Comparison of experimental vs. calculated SAXS curves (*Left*) and RDC data (*Right*) for SAXS-only refinement with an ensemble size N_e = 1 (*A*), RDC-only refinement with N_e = 1 (*B*), combined SAXS and RDC refinement with N_e = 1 (*C*), and combined SAXS and RDC refinement with N_e = 2 (*D*). The experimental and calculated (for the 10 lowest target function structures) SAXS curves are shown in black and red, respectively. Error bars: 1 SD. The RDCs for EIN$^{\alpha}$, EIN$^{\alpha/\beta}$, and EIC are color-coded blue, light blue, and red, respectively.

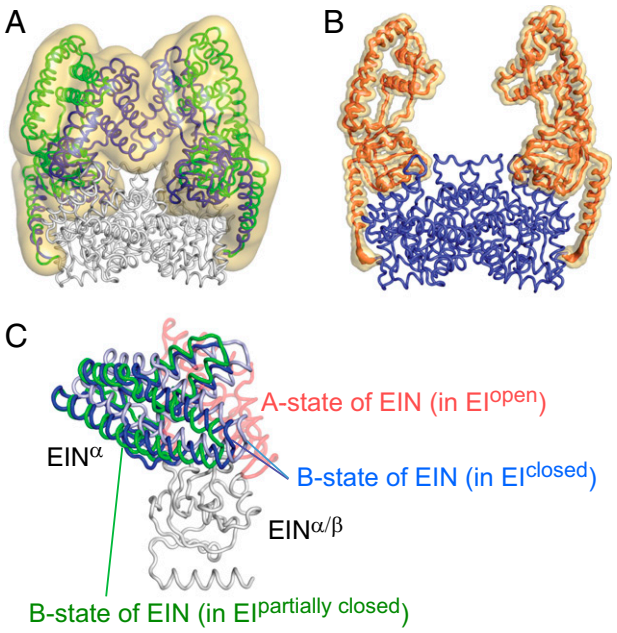

Fig. 3. Structural ensemble of the EI^{A}–PEP complex obtained from combined refinement against SAXS and RDC data for N_e = 2. (*A*) Overall distribution of EIN relative to EIC displayed as a reweighted atomic probability density map plotted at 2% (transparent yellow surface) of maximum. EIC is shown as a white ribbon. Conformations adopted by EIN in the EI^{closed} and EI$^{partially\ closed}$ states are shown as blue and green ribbons, respectively. (*B*) Backbone atomic probability density map (plotted at 50% and 2% of maximum in transparent red and yellow, respectively) for EI$^{partially\ closed}$ generated from the N_e = 2 calculations. (*C*) Orientation of EIN$^{\alpha}$ relative to EIN$^{\alpha/\beta}$ (white ribbon). EIN$^{\alpha}$ in EI^{open}, EI^{closed}, and EI$^{partially\ closed}$ is displayed in red (transparent), dark blue/light blue (for the two subunits of the X-ray structure of EI^{closed}), and green, respectively. The C$^{\alpha}$ rms difference between EIN$^{\alpha}$ of EI$^{partially\ closed}$ (green) and EI^{closed} (dark blue) is smaller than the C$^{\alpha}$ rms difference between the dark-blue and light-blue EIN$^{\alpha}$ subdomains of EI^{closed}: 3.2 Å vs. 5.6 Å (Table S1).

Three calculations were carried out with an ensemble size of N_e = 1 (i.e., a single dimeric structure) and symmetry imposed (Figs. 2 and 3 and Table 2; details of symmetry restraints are provided in *SI Materials and Methods*). Refinement against only the SAXS data results in a structure that satisfies the SAXS curve reasonably well (χ^2 = 2.1) but fails to account for the RDC data (*R*-factor ~68%) (Fig. 2*A*); refinement against only the RDC data results in a structure that satisfies the RDC data (*R*-factor = 22%) but fails to reproduce the SAXS data (χ^2 = 30) (Fig. 2*B*); and combined SAXS and RDC refinement results in a reasonable RDC *R*-factor (23%) but still fails to satisfy the SAXS data within experimental error (χ^2 = 6.7) (Fig. 2*C*). One can therefore conclude that the EI^{A}–PEP complex in solution must adopt several conformations because a single-structure representation does not simultaneously reproduce the experimental RDC and SAXS data. Interconversion between these multiple conformations must be fast on the chemical shift time scale (i.e., submilliseconds) because only a single set of cross-peaks is observed in the ^{1}H-^{15}N TROSY correlation

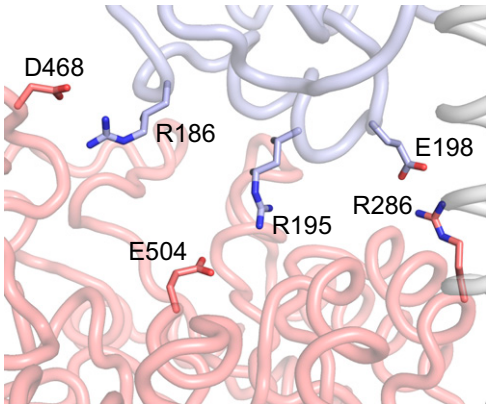

Fig. 4. Interdomain contacts between EIN and EIC in $EI^{partially\ closed}$. EIN and EIC are shown as light blue and light red ribbons, respectively, and pertinent side chains involved in potential electrostatic interdomain interactions are shown as sticks.

spectrum. The existence of fast interdomain dynamics is also supported by the observation that the magnitudes of the axial component of the alignment tensor (D_a^{NH}) for EIN^{α} and $EIN^{\alpha/\beta}$ (−19 to −20 Hz) are systematically 10–15% smaller than the magnitudes for EIC (−22 Hz) (Table 1) (27).

We therefore carried out two further joint SAXS/RDC refinement calculations with ensemble sizes of $N_e = 2$ and $N_e = 3$ (Figs. 2 and 3 and Table 2). In these calculations, the subdomains and domains of one member of the ensemble were allowed to move as rigid bodies just as in the case of the $N_e = 1$ calculations; for the $N_e = 2$ calculation, the other ensemble member was held fixed to the closed structure throughout, whereas for the $N_e = 3$ calculation, the two other members of the ensemble were fixed to the open and closed structures throughout. The population weights for the ensemble members were continually optimized at every step of molecular dynamics and minimization. The $N_e = 2$ calculation resulted in an ensemble that fully satisfied both the RDC (R-factor = 22.4 ± 0.1%) and SAXS ($\chi^2 = 1.0 \pm 0.0$) data within experimental error (Fig. 2*D* and Table 2). The addition of a third member, fixed to the open structure, results in no improvement in agreement with the SAXS data ($\chi^2 = 1.0 \pm 0.0$) and only a minimal reduction in the RDC R-factor (22.1 ± 0.1%), which is within the accuracy of the computation of the alignment tensor from molecular coordinates (24); the optimized population of the open state is ∼2%, from which one can conclude that the open state of the EI^A–PEP complex, if present at all, is essentially undetectable from the current data. In addition, it is worth noting that although the data are dominated by two distinct conformational states, each conformation is likely itself not rigid but rather a narrower ensemble of conformations.

The structure of the refined ensemble member in both the $N_e = 2$ and $N_e = 3$ calculations is best described as a partially closed state (Fig. 3 *A* and *B*). The orientation of EIN^{α} to $EIN^{\alpha/\beta}$ is very similar to the orientation in the closed state (i.e., the B conformation; Fig. 3*C*), but the position of EIN relative to EIC is more open than in the closed state (Fig. 3 *A* and *B*). The partially closed and closed states are approximately equally populated (52 ± 1% and 48 ± 1%, respectively, in the $N_e = 2$ calculation; sensitivity to population is shown in Fig. S2). The position of EIN relative to EIC in the partially closed structure is well defined, with a C^{α} rms difference to the mean of 0.4 ± 0.1 Å when best fitting to EIC (Fig. 3*C*; a discussion of domain orientation accuracy is provided in *SI Materials and Methods*). The positions of $EIN^{\alpha/\beta}$ in the partially closed and closed states are related to one another by a rotation of 14–16° and a translation of ∼6.5 Å (Table S1).

The outward displacement of $EIN^{\alpha/\beta}$ relative to EIC in the partially closed structure results in a decrease in buried accessible surface at the $EIN^{\alpha/\beta}$/EIC interface from ∼890 $Å^2$ in the closed state to ∼260 $Å^2$ in the partially closed state. Despite the large reduction in the $EIN^{\alpha/\beta}$/EIC interface, the position of $EIN^{\alpha/\beta}$ in the partially closed state is stabilized by electrostatic interactions between three Arg-Asp pairs (Arg186-Asp468, Arg195-Glu504, and Glu198-Arg286; Fig. 4).

The outward displacement of EIN in the partially closed structure of the EI^A–PEP complex relative to the closed structure effectively displaces the side chain at position 189 out of the PEP binding pocket on EIC such that in-line phosphoryl transfer of the phosphoryl group from PEP to a His at position 189 (in $EIN^{\alpha/\beta}$) can no longer occur. Of note is the fact that PEP is solvent-accessible in both the open and partially closed structures (Fig. 5 *A* and *B*, respectively) but is buried in the closed structure (Fig. 5*C*). Thus, PEP would not be able to gain access to its binding site in the closed conformation, whereas the PEP binding site is accessible to PEP in both the open and partially closed states. Similarly, the product of PEP hydrolysis, pyruvate, cannot be released directly from the closed state. These observations suggest that the partially closed structure of the EI^A–PEP complex determined here represents an intermediate in the transition from the closed state to the open state (16), that binding of PEP to apo EI^A may involve in part conformational selection of a sparsely populated species corresponding to the partially closed state, and that release of pyruvate during the course of the catalytic cycle may occur from the partially closed state.

In the partially closed state, reorientation of EIN^{α} relative to $EIN^{\alpha/\beta}$ from the B conformation to the A conformation (found in the fully open state) still results in a steric clash between EIN^{α} and EIC in the absence of further outward movement of $EIN^{\alpha/\beta}$. Hence, the partially closed-to-open transition requires additional concerted reorientation of $EIN^{\alpha/\beta}$ relative to EIC to allow the A conformation of EIN to be fully adopted.

Concluding Remarks

We have shown through combined use of SAXS and RDC measurements, coupled with simulated annealing refinement, that the EI^A–PEP complex exists in a dynamic equilibrium between closed and partially closed states with interconversion on the submillisecond time scale. Although the closed state of EI^{WT}, in the form of a phosphoryl transfer intermediate, was fortuitously selected by crystallization (14), both the closed and partially closed states of the wild-type protein are very sparsely populated in solution and their presence cannot be ascertained by SAXS or RDCs (16, 19). Thus, mutation of the active site residue at position 189 from His to Ala unveils functionally important interconverting states of EI that are undetectable in the wild type owing to their very low occupancies. Because the open-to-closed transition requires two large (∼50–90°) rigid body domain reorientations (16), the partially closed state likely represents an intermediate between the transient closed state required for

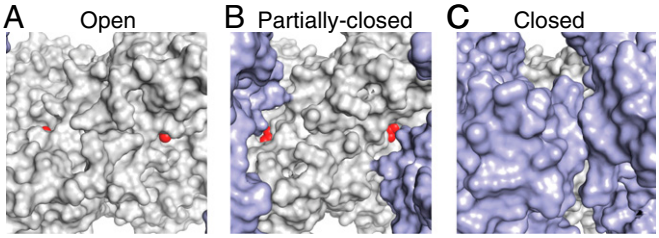

Fig. 5. Close-up view of the PEP binding sites (one per subunit) in EI^{open} (*A*), $EI^{partially\ closed}$ (*B*), and EI^{closed} (*C*). EIN and EIC are colored light blue and light gray, respectively. PEP molecules are shown as red spheres.

autophosphorylation by PEP and the predominant open state in solution needed to effect subsequent phosphoryl transfer to the downstream partner protein HPr.

From a purely experimental perspective, the existence of a dynamic equilibrium between two distinct states of the EI^A–PEP complex could not be ascertained from SAXS or RDC measurements alone because these data, when treated independent of one another, can each be accounted for reasonably well by a single-structure representation. It is only when the SAXS and RDC data are treated together that the existence of a conformational ensemble consisting of two distinct states is revealed, thereby unambiguously demonstrating the dynamic character of the EI^A–PEP complex.

Materials and Methods

Protein Expression and Purification. The H189A mutant of *E. coli* EI (EI^A) was created using the QuikChange Site-Directed Mutagenesis Kit (Stratagene) and expressed and purified as described for EI^{WT} (16).

SAXS. SAXS data were acquired at the Advanced Photon Source (Argonne National Laboratory) on samples of EI^A (5 mg/mL corresponding to ~40 μM dimer) in 20 mM Tris buffer (pH 7.4), 100 mM NaCl, 10 mM DTT, 4 mM $MgCl_2$, 1 mM EDTA, and one tablet of protease inhibitor mixture (Sigma*FAST* S8830; Sigma–Aldrich). PEP was added to a final concentration of 20 mM immediately before data acquisition (details are provided in *SI Materials and Methods*).

NMR Spectroscopy. NMR samples contained 0.4 mM subunits of EI^A, 50 mM PEP, 20 mM Tris buffer (pH 7.4), 100 mM NaCl, 4 mM $MgCl_2$, 1 mM EDTA, 2 mM DTT, and 90% H_2O/10% D_2O (vol/vol). Samples were aligned in dimyristoylphosphatidyl-choline/06:0 diether phosphatidylcholine bicelles (q = 3; Avanti Polar Lipids) doped with 0.1% 1,2-dimyristoyl-*sn*-glycero-3-phosphoethanolamine-*N*-poly(ethylene glycol)2000 (Avanti Polar Lipids) to improve bicelle stability (22). All NMR spectra were recorded at 37 °C at a spectrometer frequency of 800 MHz (details are provided in *SI Materials and Methods*).

Structure Calculations. SAXS- and RDC-driven conjoined rigid body/torsion angle/Cartesian simulated annealing was carried out in Xplor-NIH (16, 28, 29) (details are provided in *SI Materials and Methods*). Coordinates, experimental restraints, and chemical shift assignments have been deposited in the PDB (PDB ID code 2N5T).

ACKNOWLEDGMENTS. We thank Drs. Lixin Fan (National Cancer Institute) and Xiaobing Zuo (Argonne National Laboratory) for their support at the SAXS beamline. This work was supported by the Intramural Programs of the National Institute for Diabetes and Digestive and Kidney Diseases (G.M.C.) and the Center for Information Technology (C.D.S.) at the National Institutes of Health, and by the AIDS Targeted Antiviral Program of the Office of the Director of the National Institutes of Health (G.M.C.).

1. Clore GM, Venditti V (2013) Structure, dynamics and biophysics of the cytoplasmic protein-protein complexes of the bacterial phosphoenolpyruvate: Sugar phosphotransferase system. *Trends Biochem Sci* 38(10):515–530.
2. Doucette CD, Schwab DJ, Wingreen NS, Rabinowitz JD (2011) α-Ketoglutarate coordinates carbon and nitrogen utilization via enzyme I inhibition. *Nat Chem Biol* 7(12):894–901.
3. Venditti V, Ghirlando R, Clore GM (2013) Structural basis for enzyme I inhibition by α-ketoglutarate. *ACS Chem Biol* 8(6):1232–1240.
4. Chauvin F, Brand L, Roseman S (1994) Sugar transport by the bacterial phosphotransferase system. Characterization of the Escherichia coli enzyme I monomer/dimer transition kinetics by fluorescence anisotropy. *J Biol Chem* 269(32):20270–20274.
5. Chauvin F, Brand L, Roseman S (1996) Enzyme I: The first protein and potential regulator of the bacterial phosphoenolpyruvate: Glycose phosphotransferase system. *Res Microbiol* 147(6-7):471–479.
6. Chauvin F, Fomenkov A, Johnson CR, Roseman S (1996) The N-terminal domain of Escherichia coli enzyme I of the phosphoenolpyruvate/glycose phosphotransferase system: molecular cloning and characterization. *Proc Natl Acad Sci USA* 93(14): 7028–7031.
7. Liao DI, et al. (1996) The first step in sugar transport: crystal structure of the amino terminal domain of enzyme I of the E. coli PEP: sugar phosphotransferase system and a model of the phosphotransfer complex with HPr. *Structure* 4(7):861–872.
8. Garrett DS, et al. (1997) Solution structure of the 30 kDa N-terminal domain of enzyme I of the Escherichia coli phosphoenolpyruvate:sugar phosphotransferase system by multidimensional NMR. *Biochemistry* 36(9):2517–2530.
9. Garrett DS, Seok YJ, Peterkofsky A, Gronenborn AM, Clore GM (1999) Solution structure of the 40,000 Mr phosphoryl transfer complex between the N-terminal domain of enzyme I and HPr. *Nat Struct Biol* 6(2):166–173.
10. Patel HV, et al. (2006) Properties of the C-terminal domain of enzyme I of the Escherichia coli phosphotransferase system. *J Biol Chem* 281(26):17579–17587.
11. Seok YJ, Zhu PP, Koo BM, Peterkofsky A (1998) Autophosphorylation of enzyme I of the Escherichia coli phosphoenolpyruvate:sugar phosphotransferase system requires dimerization. *Biochem Biophys Res Commun* 250(2):381–384.
12. Oberholzer AE, et al. (2005) Crystal structure of the phosphoenolpyruvate-binding enzyme I-domain from the Thermoanaerobacter tengcongensis PEP: sugar phosphotransferase system (PTS). *J Mol Biol* 346(2):521–532.
13. Venditti V, Clore GM (2012) Conformational selection and substrate binding regulate the monomer/dimer equilibrium of the C-terminal domain of Escherichia coli enzyme I. *J Biol Chem* 287(32):26989–26998.
14. Teplyakov A, et al. (2006) Structure of phosphorylated enzyme I, the phosphoenolpyruvate:sugar phosphotransferase system sugar translocation signal protein. *Proc Natl Acad Sci USA* 103(44):16218–16223.
15. Oberholzer AE, Schneider P, Siebold C, Baumann U, Erni B (2009) Crystal structure of enzyme I of the phosphoenolpyruvate sugar phosphotransferase system in the dephosphorylated state. *J Biol Chem* 284(48):33169–33176.
16. Schwieters CD, et al. (2010) Solution structure of the 128 kDa enzyme I dimer from Escherichia coli and its 146 kDa complex with HPr using residual dipolar couplings and small- and wide-angle X-ray scattering. *J Am Chem Soc* 132(37):13026–13045.
17. Takayama Y, Schwieters CD, Grishaev A, Ghirlando R, Clore GM (2011) Combined use of residual dipolar couplings and solution X-ray scattering to rapidly probe rigid-body conformational transitions in a non-phosphorylatable active-site mutant of the 128 kDa enzyme I dimer. *J Am Chem Soc* 133(3):424–427.
18. Suh JY, Cai M, Clore GM (2008) Impact of phosphorylation on structure and thermodynamics of the interaction between the N-terminal domain of enzyme I and the histidine phosphocarrier protein of the bacterial phosphotransferase system. *J Biol Chem* 283(27):18980–18989.
19. Venditti V, Tugarinov V, Schwieters CD, Grishaev A, Clore GM (2015) Large interdomain rearrangement triggered by suppression of micro- to millisecond dynamics in bacterial Enzyme I. *Nat Commun* 6:5960.
20. Bax A, Grishaev A (2005) Weak alignment NMR: A hawk-eyed view of biomolecular structure. *Curr Opin Struct Biol* 15(5):563–570.
21. Clore GM (2000) Accurate and rapid docking of protein-protein complexes on the basis of intermolecular nuclear overhauser enhancement data and dipolar couplings by rigid body minimization. *Proc Natl Acad Sci USA* 97(16):9021–9025.
22. King V, Parker M, Howard KP (2000) Pegylation of magnetically oriented lipid bilayers. *J Magn Reson* 142(1):177–182.
23. Fitzkee NC, Bax A (2010) Facile measurement of ^1H-^{15}N residual dipolar couplings in larger perdeuterated proteins. *J Biomol NMR* 48(2):65–70.
24. Zweckstetter M, Bax A (2000) Prediction of sterically induced alignment in a dilute liquid crystalline phase: Aid to protein structure determination by NMR. *J Am Chem Soc* 122(15):3791–3792.
25. Huang JR, Grzesiek S (2010) Ensemble calculations of unstructured proteins constrained by RDC and PRE data: A case study of urea-denatured ubiquitin. *J Am Chem Soc* 132(2):694–705.
26. Deshmukh L, et al. (2013) Structure and dynamics of full-length HIV-1 capsid protein in solution. *J Am Chem Soc* 135(43):16133–16147.
27. Braddock DT, Cai M, Baber JL, Huang Y, Clore GM (2001) Rapid identification of medium- to large-scale interdomain motion in modular proteins using dipolar couplings. *J Am Chem Soc* 123(35):8634–8635.
28. Schwieters CD, Clore GM (2014) Using small angle solution scattering data in Xplor-NIH structure calculations. *Prog Nucl Magn Reson Spectrosc* 80(1):1–11.
29. Schwieters CD, Kuszewski J, Clore GM (2006) Using Xplor-NIH for NMR molecular structure determination. *Prog Nucl Magn Reson Spectrosc* 48(1):47–62.
30. Clore GM, Garrett DS (1999) *R*-factor, free *R* and complete cross-validation for dipolar coupling refinement of NMR structures. *J Am Chem Soc* 121(39):9008–9012.
31. Delaglio F, et al. (1995) NMRPipe: A multidimensional spectral processing system based on UNIX pipes. *J Biomol NMR* 6(3):277–293.
32. Schwieters CD, Clore GM (2001) Internal coordinates for molecular dynamics and minimization in structure determination and refinement. *J Magn Reson* 152(2): 288–302.
33. Bermejo GA, Clore GM, Schwieters CD (2012) Smooth statistical torsion angle potential derived from a large conformational database via adaptive kernel density estimation improves the quality of NMR protein structures. *Protein Sci* 21(12): 1824–1836.
34. Ryabov Y, Suh JY, Grishaev A, Clore GM, Schwieters CD (2009) Using the experimentally determined components of the overall rotational diffusion tensor to restrain molecular shape and size in NMR structure determination of globular proteins and protein-protein complexes. *J Am Chem Soc* 131(27):9522–9531.
35. Renka RJ (1984) Interpolation of data on the surface of a sphere. *ACM Trans Math Softw* 10(4):417–436.
36. Grishaev A, Guo L, Irving T, Bax A (2010) Improved fitting of solution X-ray scattering data to macromolecular structures and structural ensembles by explicit water modeling. *J Am Chem Soc* 132(44):15484–15486.

Supporting Information

Venditti et al. 10.1073/pnas.1515366112

SI Materials and Methods

NMR Spectroscopy. All NMR spectra were recorded at 37 °C on a Bruker 800-MHz spectrometer equipped with a *z*-shielded gradient triple-resonance cryoprobe. Spectra were processed using NMRPipe (31) and analyzed using the program SPARKY (https://www.cgl.ucsf.edu/home/sparky/). Backbone amide ($^1D_{NH}$) RDCs were measured using the ARTSY (amide RDCs by TROSY) technique (23) and analyzed using Xplor-NIH (29). Cross-peak assignments of the ^{1}H-^{15}N TROSY correlation spectrum of the EI^A–PEP complex were taken from our previous study by Venditti et al. (19). The latter were obtained by first transferring the assignments obtained for isolated EIN (8) and EIC (13) onto the spectrum of EI^A, followed by PEP titration experiments in which cross-peak positions were followed as a function of added ligand (19).

SAXS Data Collection. SAXS data were collected on beamline 12-ID-B (allocated under the PUP-24152 agreement between the National Cancer Institute and Argonne National Laboratory) at the Advanced Photon Source [Argonne National Laboratory (supported by the Department of Energy under Contract DE-AC02-06CH11357)]. Data collection was done using a Dectris Pilatus 2M detector positioned 3 m from the sample capillary in a highly offset geometry with respect to the incident beam. X-ray radiation with energy of 14 keV was used, resulting in an observable *q*-range of 0.01–0.80 Å^{-1}. Scattered radiation was detected subject to a 13-keV low-energy cutoff. *q*-axis mapping was done using scattering from a silver behenate standard sample. Totals of 20 sequential data frames with exposure times of 2 s were recorded with the samples at 5.0, 2.5, and 1.25 mg/mL and kept at 25 °C throughout the measurement. To prevent radiation damage, volumes of 100 μL of samples and buffers were oscillated during data collection using a flow-through setup. Individual data frames were masked, corrected for detector sensitivity, radially integrated, and normalized by the corresponding incident beam intensities. The final 1D scattering profiles and their uncertainties were calculated as means and mean uncertainties over the 20 individual frames. Subtraction of the buffer data and analysis of the scattering profiles were carried out as described (28) in Xplor-NIH (29) using the calcSAXS-bufSub helper function (19).

Structure Calculations. EI is composed of two domains, EIN (residues 1–254) and EIC (residues 262–573), with a linker region between them; EIN is further decomposed into two subdomains, EIN$^\alpha$ (residues 25–142) and EIN$^{\alpha/\beta}$ (residues 1–21 and 147–230) and a swivel helix (residues 234–254). Coordinates for the closed structure, EI^{closed}, were constructed from the crystal structure of the phosphoryl transfer intermediate [PDB ID code 2HWG (14)], where the coordinates of EIN$^\alpha$ and EIN$^{\alpha/\beta}$ were taken from the solution structure of the EIN–HPr complex [PDB ID code 3EZA (9)] because those coordinates better fit the RDC data. Coordinates for the linker regions between EIN$^\alpha$, EIN$^{\alpha/\beta}$, and the swivel helix were obtained by minimizing covalent and atomic overlap energy terms. The coordinates for the open structure, EI^{open} (derived by SAXS- and RDC-driven rigid body simulated annealing), were taken directly from PDB ID code 2KX9 (16); as in the case of the closed structure, the coordinates for the EIN$^\alpha$ and EIN$^{\alpha/\beta}$ subdomains are the coordinates from PDB ID code 3EZA, whereas the coordinates for the swivel helix and EIC domain are from PDB ID code 2HWG.

For the $N_e = 1$ calculations, the initial coordinates were taken to be the closed structure described above; for the $N_e = 2$ calculation, the closed structure is used for the initial coordinates of both ensemble members; and for the $N_e = 3$ calculation, the open structure is used for the initial coordinates of one ensemble member, whereas the closed structure is used for the initial coordinates of the other two members.

Molecular dynamics and gradient minimization were performed using the general internal variable dynamics (IVM) module (IVM facility) (32) with an automatically adjustable integration step size in Xplor-NIH (29). For the $N_e = 2$ calculation, the backbone of one ensemble member is held fixed to the close structure throughout; for the $N_e = 3$ calculation, the backbones of two of the ensemble members are held fixed, one to the open structure and the other to the closed structure. For the ensemble member whose structure is optimized, the EIN domains are grouped as rigid bodies throughout the high-temperature dynamics and simulated annealing portions of the calculation, and the following two components of the EIN domains were allowed to move as rigid bodies during final gradient minimization: the EIN$^\alpha$ subdomains and the EIN$^{\alpha/\beta}$ subdomains grouped with the neighboring swivel helices. Additionally, all side chains were give torsion degrees of freedom during final gradient minimization. Throughout the entire calculation, linker regions were allowed Cartesian degrees of freedom.

Broad backbone torsion angle restraints were used to ensure that the backbone of residues in the linker regions lie within the allowed regions of the Ramachandran map. The ensemble member whose structure is refined during the course of the calculations is restrained to be symmetric using the PosDiffPot energy term with a force constant geometrically ramped from 0.001 to 0.1 kcal·mol^{-1}·Å^{-2} during simulated annealing, combined with a distance symmetry term applied with the DistSymmPot energy term with a force constant ramped from 0.1 to 10 kcal·mol^{-1}·Å^{-2}. [Note that the fully open EI structure, EI^{open}, is symmetric (16), whereas the position of the EIN$^\alpha$ subdomains is slightly asymmetric in the closed structure, EI^{closed}, due to asymmetric intersubunit contacts between the EIN$^\alpha$ subdomains in the crystal structure (14)]. An additional PosDiffPot energy term was applied to the EIN domains, restraining them to lie within 5 Å of the closed X-ray structure with a force constant of 10 kcal·mol^{-1}·Å^{-2} throughout. A multidimensional torsion angle database potential of mean force (33) was applied in two terms: the first with a force constant ramped from 0.001 to 2 kcal·mol^{-1}, whereas the second, applied solely to linker backbone degrees of freedom, was given a larger force constant ramped from 0.001 to 10 kcal·mol^{-1}. A knowledge-based, low-resolution hydrophobic contact potential, the residueAffPot term (34), was used to help guide any potential interactions between subunits. The RDC data were fit using the SARDCPot term (25), which computes the alignment tensor from molecular structure, and is appropriate only for alignment media (e.g., the neutral bicelles used here) for which electrostatic interactions between the protein and the aligning medium are negligible. The scale factor for the SARDC term is a fit parameter that is optimized at every time step of dynamics and minimization. A single RDC was measured for residue 143 in the linker region between the EIN$^\alpha$ and EIN$^{\alpha/\beta}$ subdomains, and it was included in the structure calculations but not in the RDC *R*-factors reported in Tables 1 and 2 because this RDC does not have a well-defined target value. Because there were fewer measured RDCs for EIC, the force constant applied to those terms was double the force constant applied to the EIN RDCs. The value of the latter RDC force constant was 0.15 kcal·mol^{-1}, with a linear potential shape during high-temperature dynamics and ramped from 0.6 to 6 kcal·mol^{-1} with a quadratic potential during simulated annealing. SAXS restraints were included using the solnScatPot facility (28), with the treatment of rigid bodies detailed in the next section. The SAXS force constant was set to 75 kcal·mol^{-1} during high-temperature dynamics and ramped from 75 to 750 kcal·mol^{-1} during simulated annealing.

In addition to the above potential terms, the target function included the various standard terms for covalent geometry (bonds, angles, and improper torsions) and a quartic repulsive van der Waals nonbonded term to prevent atomic overlap (29). During the first round of high-temperature dynamics, the nonbonded term was disabled, whereas for the second and third rounds, all interactions were taken into account aside from those interactions involving the side chain atoms of the linker between EIN and EIC. During simulated annealing, interactions between all atoms were enabled and the force constant for the nonbonded term was ramped from 0.5 to 4 kcal·mol^{-1}·Å^{-4}, whereas the radius multiplier was scaled from 0.9 to 0.8.

The relative population of ensemble members present in the SAXS and RDC measurements was assumed to be the same, and was determined during structure calculations using the facility described by Schwieters and Clore (28). To avoid instabilities where an ensemble population would go to zero, a stabilizing term (28) was used with a force constant ramped down from 100 to 0.2 kcal·mol^{-1} during simulated annealing.

The structure calculation commenced by randomizing velocities of the active degrees of freedom. The masses of each atom in the linker regions and the atomic masses of the entire EIN$^{\alpha}$ and EIN$^{\alpha/\beta}$ subdomains were set to 100 atomic mass units (daltons). Three rounds of high-temperature dynamics were performed at 3,000 K for the lesser of 800 ps or 8,000 steps. For the first two rounds, the linear SARDC potential was used with a force constant of 0.15 kcal·mol^{-1}, whereas for the final round of high-temperature dynamics, a quadratic SARDC potential was used with a force constant of 0.06 kcal·mol^{-1}. In simulated annealing, the initial and final temperatures were 3,000 K and 25 K, respectively, with the temperature decreasing in increments of 25 K. At each temperature of simulated annealing, molecular dynamics were run for the shorter of 0.4 ps or 200 steps.

For each calculation, a set of 200 ensembles was calculated and the 10 ensembles with the lowest target function (energy) values were selected for further analysis. The full Xplor-NIH script used for the structure calculations in the current paper is available in the Xplor-NIH distribution, which can be downloaded from nmr.cit.nih.gov/xplor-nih.

Solution Scattering of Rigid Bodies. The X-ray scattering curves $I(q)$ were calculated from atomic coordinates, as described by Schwieters and Clore (28). In this approach, the scattering amplitude contribution of each atom (or glob) $A(\mathbf{q})$ is computed at points in reciprocal space $\mathbf{q}$ on spheres of constant amplitude q, leading to computational cost scaling as $N_a \times N_s \times N_q$, where N_a is the number of atoms, N_s is the number of points on the reciprocal space sphere, and N_q is the number of scattering amplitude points q for which I is evaluated. Typically, N_s ~500 and N_q ~50. Although computation of $I(q)$ scales linearly with the number of atoms, this calculation becomes costly for large systems. For atoms within a rigid body, the relative atom positions do not change; thus, after an initial calculation, the corresponding contribution to the scattering amplitude can be computed without referring to atomic positions. If $\mathbf{r}_j'$ is the atomic position of atom j after displacement of the rigid body with the initial position given by $\mathbf{r}_j$, then

$$\mathbf{r}_j' = R\mathbf{r}_j + \Delta\mathbf{r}, \qquad \text{[S1]}$$

where R and $\Delta\mathbf{r}$ describe the rotation and translation of the rigid body, respectively. The corresponding rigid body scattering amplitude is:

$$A_{\text{rigid}}(\mathbf{q};\{\mathbf{r}\}) = e^{i\Delta\mathbf{r}\cdot\mathbf{q}} A^0_{\text{rigid}}(\mathbf{q}';\{\mathbf{r}\}), \qquad \text{[S2]}$$

where $\{\mathbf{r}\}$ denotes the dependence on the set of initial atomic coordinates and

$$\mathbf{q}' = R^T\mathbf{q}. \qquad \text{[S3]}$$

In practice, $A_{\text{rigid}}(\mathbf{q};\{\mathbf{r}\})$ is computed using a spline over a spherical surface of constant q to evaluate $A^0_{\text{rigid}}(\mathbf{q}';\{\mathbf{r}\})$, the scattering amplitude at the initial atomic position, but with rotated scattering vector amplitude, $\mathbf{q}'$. Interpolation on the surface of a sphere was implemented using the algorithm of Renka (35).

The above formulation yields vast speedups when a calculation can be decomposed into a small number of rigid bodies, because the computation time becomes independent of the number of atoms. The solnScatPot facility of Xplor-NIH used to calculate solution scattering curves from atomic coordinates (28) has been extended such that rigid regions can be simply indicated in input scripts using the addRigidRegion method of solnScatPot objects. Scattering amplitudes of the rigid regions are evaluated once and then updated via the algorithm described above during molecular dynamics and gradient minimization calculations.

SAXS Background Subtraction. Subtraction of SAXS buffer scattering was performed in concert with structure determination using an adaptation of the AXES algorithm (36) described by Venditti et al. (19). The function solnScatPotTools.fitSolventBuffer was called before high-temperature dynamics and at each temperature in simulated annealing before performing molecular dynamics to determine the coefficient of buffer scattering (a), the amount of isotropic background scattering (c), and the effective density of surface-bound solvent (ρ_b) to be used in the following calculations.

We note that in this background subtraction procedure, the experimental SAXS curve depends on the input structure, such that it is (subtly) different in the various panels of Fig. 2. For this reason, for the SAXS fits to structures far from the correct structure shown in Fig. 1, a standard SAXS fitting approach (28) was used, taking as the experimental SAXS curve the result from the lowest energy structure of the $N_e = 2$ ensemble calculation.

Estimation of Domain Orientation Accuracy for the Partially Closed State. Relative domain orientations are primarily determined by the RDC data. To obtain a handle on the accuracy with which the relative domain orientations in the partially closed state are determined, we carried out a series of calculations in which random noise (±2 Hz) was added to the experimental RDCs, with a different distribution of random noise for each ensemble calculated. This approach serves to address not only the effects of errors in the measured RDCs themselves but also intrinsic uncertainties in the calculation of the alignment tensors from atomic coordinates. A total of 200 $N_e = 2$ ensembles were calculated, and the 10 lowest energy structures were analyzed. Although the precision (C$^{\alpha}$ atomic rms difference to the mean coordinate positions) with which the position of EIN is determined (when best-fitting to EIC) is reduced from 0.4 to 0.7 Å upon addition of RDC noise, the C$^{\alpha}$ rms difference between the mean coordinates for EIN calculated with and without added RDC noise is only 0.2 Å (when best-fitting to EIC). Furthermore, the populations of the partially closed and closed states remain unchanged within error (52.2 ± 1.3% and 47.8 ± 1.3%, respectively, with added RDC noise, vs. 51.7 ± 1.1% and 48.3 ± 1.1%, respectively, with no noise). Finally, the SAXS χ^2 (1.00 ± 0.02) and RDC R-factors (22.3 ± 0.1%, 20.2 ± 0.4%, 25.4 ± 0.2%, and 22.5 ± 0.2% for EIN$^{\alpha}$, EIN$^{\alpha/\beta}$, EIC, and the whole EI^{A}, respectively) for the structures calculated with RDC noise are essentially unchanged relative to those structures calculated without added noise (Table 2).

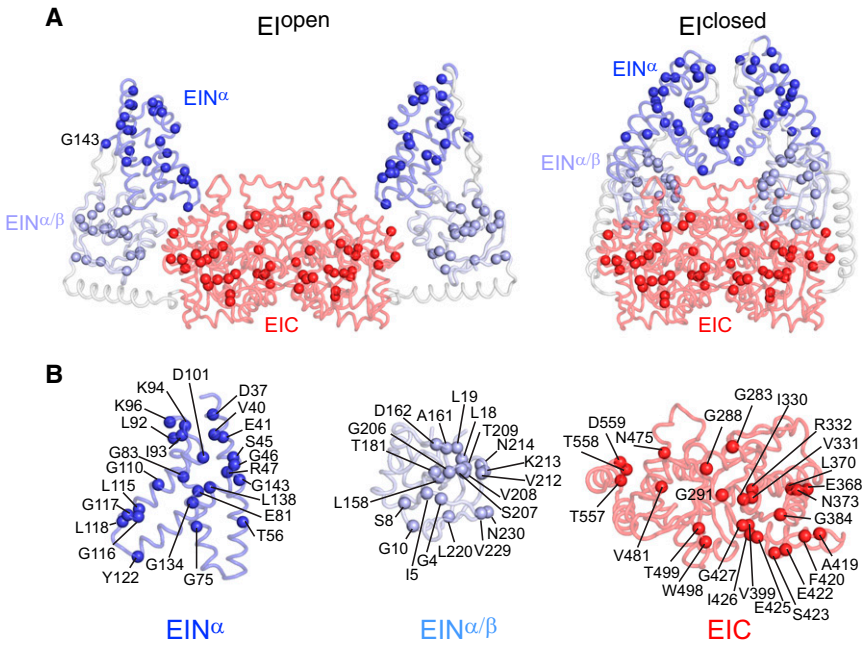

Fig. S1. Distribution of measured $^1D_{NH}$ RDCs on the structure of EI. The backbone nitrogen atoms for which corresponding $^1D_{NH}$ RDCs have been measured are indicated by color-coded spheres: dark blue indicates EIN$^{\alpha}$, light blue indicates EIN$^{\alpha/\beta}$, and red indicates EIC. (*A*) Open (*Left*) and closed (*Right*) structures of EI. (*B*) Individual subdomains/domains with EIN$^{\alpha}$ (*Left*), EIN$^{\alpha/\beta}$ (*Middle*), and EIC (*Right*). Note the RDC for Gly143 was included in the structure calculations but omitted from the statistics reported in Tables 1 and 2 because Gly143 is in a linker region, and hence does not have a well-defined target value (*SI Materials and Methods*).

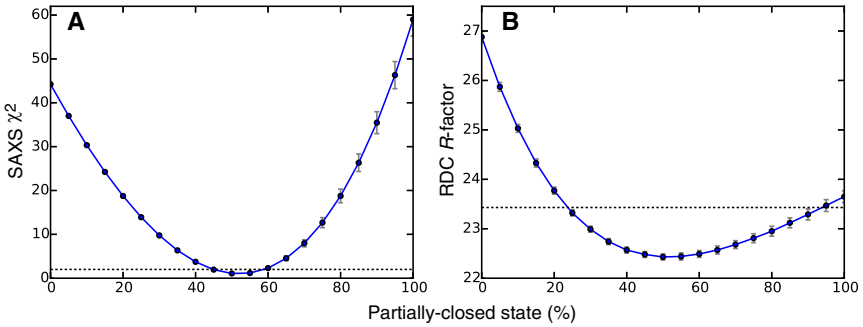

Fig. S2. Sensitivity of SAXS (*A*) and RDC (*B*) data to the population of partially closed and closed states. The points represent averages over the top 10 calculated ensembles, with manually specified population weights and error bars representing 1 SD. (Note the RDC *R*-factor of 26.9% at 100% of the closed state is lower than the value of 28.4% reported in Fig. 1*B* and Table 1, because all side chains are given torsional degrees of freedom during final minimization, which produces small changes in the molecular surface used to calculated the alignment tensor.) The dashed lines indicate conservative upper metrics for expected agreement with the experimental data, set to $\chi^2 = 2$ for SAXS and 23.4% for the RDC *R*-factor (1% larger than the value of 22.4% at the minimum of the curve). Within this conservative limit, the SAXS and RDC data, treated separately, confine the population of the partially closed state to a range of 45–60% and 25–95%, respectively. These data also suggest that the lower limit of detection of the partially closed state is about 10% (i.e., if the populations of partially closed and closed states were 10% and 90%, respectively, instead of being approximately equally populated, it is possible that the effect of the presence of a partially closed state would manifest itself sufficiently in the combined SAXS and RDC data to be barely detectable within the errors of the experimental data).

Table S1. Comparison of $EI^{partially\ closed}$ and EI^{closed} structures

Structure comparison	C^{α} atomic rms difference, Å	Rotation, °	Centroid translation, Å
Comparison of $EI^{partially\ closed}$ vs. EI^{closed}*			
EIN^{α} relative to $EIN^{\alpha/\beta}$	6.2 ± 0.4/2.9 ± 0.3	11.1 ± 0.7/9.4 ± 0.8	5.9 ± 0.3/2.2 ± 0.3
$EIN^{\alpha/\beta}$ relative to EIC	7.5 ± 0.2/6.9 ± 0.1	16.5 ± 0.6/13.8 ± 0.5	6.7 ± 0.1/6.2 ± 0.1
EIN relative to EIC	16.1 ± 0.2/15.8 ± 0.2	23.1 ± 0.2/15.8 ± 0.2	13.7 ± 0.2/10.9 ± 0.2
Comparison between the two subunits of EI^{closed}			
EIN^{α} relative to $EIN^{\alpha/\beta}$	5.6	5.4	5.5

In this series of comparisons, the differences in the positions of EIN^{α}, $EIN^{\alpha/\beta}$, and EIN between the $EI^{partially\ closed}$ and EI^{closed} structures are characterized in terms of C^{α} rms difference as well as rotation and translation between centroids, computed by best-fitting to $EIN^{\alpha/\beta}$, EIC, and EIC, respectively.

*First and second numbers refer to subunits A and B, respectively, of EI^{closed}. In EI^{closed}, the EIN^{α} subdomains are asymmetrically placed relative to the C_2 symmetry axis of the $EI^{\alpha/\beta}$-EIC dimer, as a consequence of asymmetric EIN^{α} intersubunit contacts (14). The average C^{α} rms differences for EIN alone between the top 10 $EI^{partially\ closed}$ structures and subunits A and B of EI^{closed} are 1.5 ± 0.1 and 1.1 ± 0.1 Å, respectively.